Electronic Supplementary Information: High-content adhesion assay to address limited cell samples

1 Materials and Methods

Device Fabrication

Established soft lithography techniques[1,2] were used to fabricate single-use microdevices (including PDMS diaphragm cover) consisting of seven independent microchannels on a 3” × 1” slide.

150-mm diameter silicon wafers were acquired from WRS Materials (San Jose, CA). Different formulations of SU-8 negative photoresist were acquired from Microchem (Newton, MA). Poly(dimethylsiloxane) (PDMS) was obtained from Dow Corning (Midland, MI). Corning #2947 glass slides and NUNC tissue culture-treated OmniTrays (#165218) were obtained from Thermo Fisher Scientific (Pittsburgh, PA). Acetone and isopropanol (IPA) were purchased from Fisher Scientific, and propylene glycol monoethyl ether acetate (PG-MEA) was purchased from Sigma-Aldrich (St. Louis, MO).

Two separate master molds were made, one for the microchannels and one for the PDMS diaphragm cover. For the microchannels, SU-8-100 was spincoated at 1500 rpm for 45 s to yield a $\sim$200 μm layer. The mold was then baked for 2 h at 95°C, UV exposed for 700 mJ/cm^2, and post-exposure baked for 90 min at 95°C. After cooling to room temperature, the next layer of SU-8-100 was spincoated at 500 rpm for 90 s to yield an additional 400 μm layer. The mold was baked for 2.5 h at 95°C, UV exposed for 2000 mJ/cm^2, post-exposure baked for 2 h min at 95°C, cooled to room temperature, and developed in PG-MEA on a rotator for a minimum of 2 h. After development, the master mold was rinsed sequentially with fresh PG-MEA, acetone, and IPA, and blown dry with compressed air. Resulting dimensions were as follows: Microchannel: 1.5 mm × 7.5 mm × 200 μm (from inside edge of input to inside edge of output). Channel input port: 1.5 mm radius. Channel output port: 6.24 mm × 5.6 mm for the major and minor axes, respectively.

For the diaphragm cover, SU-8-50 was spincoated at 2000 rpm to yield a 50 μm layer, soft-baked at 95°C for 1h, exposed for 450 mJ/cm^2, and post-exposure-baked for 30 min to create the air escape passage. SU-8-100 was spincoated at 500 rpm for 45 s to yield a $\sim$1 mm layer, soft-baked at 95°C for 5 h, exposed for 3000 mJ/cm^2, and post-exposure-baked for 2 h at 95°C to create the diaphragm air chamber. SU-8-100 was spincoated at 1250 rpm to yield a 250 μm layer, soft-baked for 5 h, exposed for 3500 mJ/cm^2, and post-exposure-baked for 2h to create the air escape ports. The wafer was developed in PG-MEA on a rotator for a minimum of 2 h. After development, the master mold was rinsed sequentially with fresh PG-MEA, acetone, and IPA, and blown dry with compressed air. Resulting dimensions were as follows: Air chamber: 7 mm × 7.8 mm × 1 mm. Air escape channel: 50 μm tall × 100 μm wide. Air escape port: 3 mm radius, 1.25 mm height.

PDMS at a 10:1 ratio of elastomer base and curing agent was mixed vigorously with a plastic fork and allowed to degas in a vacuum dessicator for $\sim$1 h. After degassing, PDMS was poured over each of the two master molds (10 g of mixed PDMS each), which were each placed on separate hot plates. Transparency film (AF4300, 3M, St. Paul, MN) was cut to size, and placed on top of the PDMS with sufficient care to not trap any bubbles. Silicone foam, a polycarbonate block, and 30 lbs of weight were then placed on top of the master mold, and the hot plate was set to 80°C for 4 h.

Once cured, the PDMS slabs were removed from the SU-8 master molds, and placed in a Soxhlet extractor to extract uncrosslinked oligomers using 100% ethanol[3]. Glass slides were rinsed in acetone and IPA, and blown dry with compressed air. OmniTrays were used as supplied. For glass-bottom devices, the PDMS microchannel and glass slide were both treated with oxygen plasma before bonding. For polystyrene-bottom devices, OmniTrays were used as supplied, and PDMS microchannel layers were passively bonded to the polystyrene surface. Immediately prior to running the assay, the PDMS cover layer was reversibly bonded to the PDMS microchannel layer using tweezers for handling.

Piezo-Actuator and Accessories

Actuation of the diaphragm was achieved using a 3.5 cm × 1.3 cm × 0.3 cm cantilever-style piezo-actuator (Q220-A4-303YB - Piezo Systems, Inc. Woburn, MA) with a small tab of plastic with cap screw secured to the end in order to provide a focused point of contact with the diaphragm. Piezo-actuation is attractive because it has no moving parts such as gears or ball bearings. Applied voltage bends the ceramic material, allowing its use in challenging environments such as incubators while operating over a large, linear dynamic range. Signals are generated using a 33220A waveform generator (Agilent Technologies Santa Clara, CA). Because the input voltage of the piezo-actuator (0-100 V) is higher than the output of the signal generator (0-10 V), a piezo amplifier was used to amplify the signal. Previous characterization of this amplifier has been performed by others[4]. The amplifier was purchased with an atypical input voltage range of ± 1.5 V to offer the ability to directly interface with the output of a computer headphone jack and enable open-source software solutions for signal generation.

Piezo-actuation of the Diaphragm

Fabricated PDMS devices were placed in a tissue-culture treated OmniTray. The diaphragm was reversibly bonded over the large output ports of the device. A metal strip was fixed to the inside of the OmniTray using double-sided tape ∼2 cm from the channels. The piezo-actuator, mounted to a 1 cm × 2.5 cm piece of plastic via double-sided tape, is held in place on the metal strip with a total of 4 magnets (K&J Magnetics B333, N52-grade neodymium 3/16" × 3/16" × 3/16" cube) fixed to the actuator assembly. The magnets provided an easy means to place and remove the actuator. The position of the actuator was able to remain very stable during manipulation of the OmniTray, enabling the flip technique for shear estimation. The cap screw used as the point of contact between the actuator and diaphragm provided height adjustability when needed. The entire assembly could be enclosed in a covered OmniTray. The lid provided enough compliance for the small wires leading to the piezo-actuator. The actuator was placed on the diaphragm just prior to experimentation. It can also be put in place earlier if desired.

A previous study by Morris and Forster[5] also used a piezo-electric actuator to produce oscillatory flow in a microchannel. They examined the differences between exact and impedance models of fluid flow. However, the piezo-actuator used by Morris and Forster was in direct contact with the fluid forming the ceiling of a reservoir, and in this arrangement, deformations in the actuator directly resulted in displacement of the fluid.

Microscope

Images were acquired with an inverted fluorescent microscope (PN:IX70 - Olympus, Center Valley, PA) equipped with a digital camera (PN:C4742-80-12AG - Hamamatsu, Hamamatsu City, Japan) and MetaMorph imaging software (Molecular Devices, Sunnyvale, CA). A Plan N 2X phase contrast objective (NA = 0.06, Olympus) was used for all images.

Piezo-Actuator Motion Measurements

Motion was measured using bright-field microscopy where the piezo-actuator was mounted on its side such that the tip appeared to move side-to-side in the field of view. Motion was quantified from digital image streams.

Piezo-Actuator Response

Fig S1 shows voltage- and frequency-response of the fully assembled actuator and tip, but without being in contact with the diaphragm. The actuator voltage response was linear, while the frequency response had constant amplitudes below 20 Hz and a resonant frequency that was greater than 80 Hz.

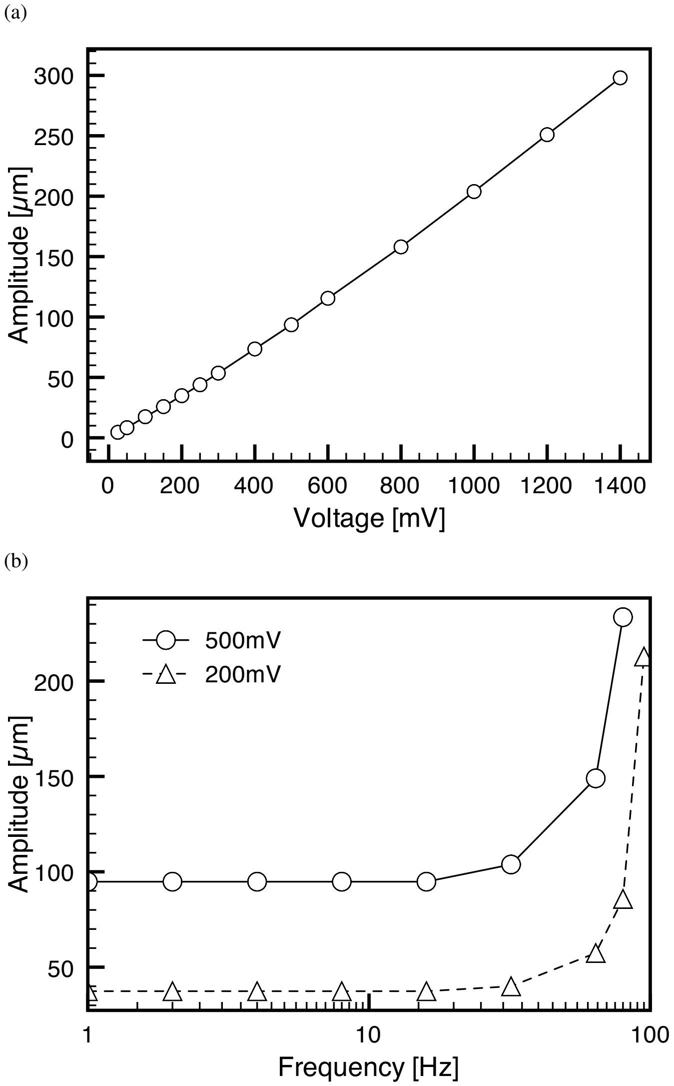

Figure S1 Experimental motion measurements of piezo amplitudes. (a) Actuator amplitude is linear to the input voltage. Voltages refer to peak-to-peak signal levels that enter the piezo amplifier. (b) Actuator amplitude was constant below 16 - 32 Hz. The resonant frequency is > 80 Hz.

It is expected that coupling of the actuator with the microchannel and membrane will alter the frequency response, likely damping the resonance observed at high frequencies. This is examined in a subsequent subsection.

Shear Stress Calibration Procedure

A shear stress calibration procedure was implemented to improve the accuracy of results in adhesion experiments, and to characterize the response of the fully assembled system to different voltages and frequencies. Shear stress at the surface of

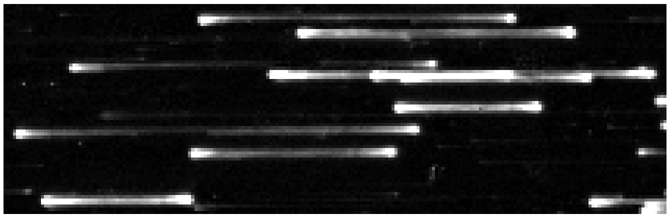

Figure S2 Calibration image streaklines. Example of streaklines in a phase contrast image that has been background subtracted to enhance contrast.

the microchannel substrate is measured based on the amplitude of motion of particles oscillating with the flow. The objective of this calibration procedure is to measure the maximum particle amplitude within the channel as the particle settles from the ceiling to the substrate, thus passing through the peak in the velocity flow profile and giving an accurate measure of the actual flow amplitudes for a given microchannel-diaphragm-actuator setup. The flow amplitudes and frequency can then be used to calculate shear stress.

The calibration process started with actuation of the fluid at the desired voltage and frequency. Subsequently, a dilute suspension of the test particles was dispensed into the channel to provide approximately 30 to 300 particles within the microscope field of view. The air escape shown in Fig 1C of the main text was filled with 7.5 μL of fluid to seal the diaphragm air chamber. The channel was focused to provide an accurate view of suspended particles. The entire device was inverted and kept upside-down for 45 s to allow the cells to settle toward the ceiling. Surface tension of the droplets kept fluid from flowing out of the microchannels. As the cells settled, the microscope was set to acquire a 90-frame image stream using phase contrast, with an exposure time chosen such that each frame captured one full oscillation (exposure time = $1/f$) of each particle. Thus, in each image the particle motion appeared as a streakline where the length of the streakline is the amplitude of cell motion (Fig S2). By imaging at least a full 360° cycle, the particle is assured of reaching the extents of its motion (i.e. the left-most and right-most position) to establish a full streakline for amplitude measurement. Acquisition of the stream was started and the device was inverted to be right-side-up and immediately placed on the microscope. This image stream captured the oscillatory motion of the cells as they settled from the ceiling to the substrate. When viewing the image streams, the streak size of each cell can be seen to increase as it gets closer to the half-height of the microchannel due to the shape of the velocity flow profile. The maximum streakline length is determined for the image stream using a particle within the center 80% of the channel (as viewed from the top), where shear stress is uniform for this device geometry.[6] The amplitude of the motion is then used to calculate the shear stress in the channel.

Given that the air escape is plugged after calibration, subsequent loading of particles into the device is aided by gentle tapping of the actuator to help introduce the particles loaded at the port into the microchannel measurement region. A dilute suspension of the experimental cells was used for calibration during cell-based experiments while 15 μm fluorescent beads (PN:F8843 - Invitrogen. Eugene, OR) were used for the technical characterization of the device.

Calculation of Shear Stress from Particle Amplitudes

To estimate shear stress from amplitudes of particle motion at the center streamline, the flow profile (parabolic or non-parabolic) must be determined. To do this, the microfluidic channel was modeled as a parallel-plate flow-chamber (PPFC). Fluid flow was simulated using a pulsatile flow model that accounts for potentially non-parabolic profiles at higher frequencies and assumes laminar flow conditions. Fig S3 (dashed line) shows that for a given maximum pressure gradient, the shear stress at the channel substrate declines as frequency is increased. This decline is due to inertial effects. Note also that flow profile is also changing slightly from parabolic to non-parabolic. Thus, to assess if we can assume a parabolic flow profile to simplify shear stress calculations during cell-based experiments, we compared the shear stress at the channel substrate calculated using either the true non-parabolic shape (dashed) or a purely parabolic profile (solid black). The ratio of the difference over the non-parabolic value is shown in gray. Thus, below a frequency of 10 Hz, the error of assuming a parabolic flow profile to calculate shear from particle amplitude is negligible. By defining particle position, x, over time using Eq. S1 where A is the amplitude of the motion at the center streamline of a parabolic flow profile, f is frequency, and t is time, parabolic flow assumptions can be used to arrive at Eq. S6 for determining shear stress, τ, at the center 80% of the channel substrate as a function of particle amplitude. Note the length of the particle streak obtained during the calibration procedure is equal to $2A$. Other variables in the list of equations are as follows; u = particle velocity, u_{max} = maximum particle velocity, $\overline{u}$ = average fluid velocity of the parabolic flow, Q = flow rate of the parabolic flow, b = width of the rectangular channel, h = height of the rectangular channel (assumed that h $\ll$ b), μ= dynamic fluid viscosity (assumed here to be 0.00078 $\mathrm{kg\,m^{-1}\,s^{-1}}$).

$$x = A\sin(2\pi ft) \tag{S1}$$

$$\frac{dx}{dt} = u = 2\pi Af\cos(2\pi ft) \tag{S2}$$

$$u_{max} = 2\pi Af \tag{S3}$$

$$\overline{u} = \frac{Q}{bh} = \frac{2}{3}u_{max} \tag{S4}$$

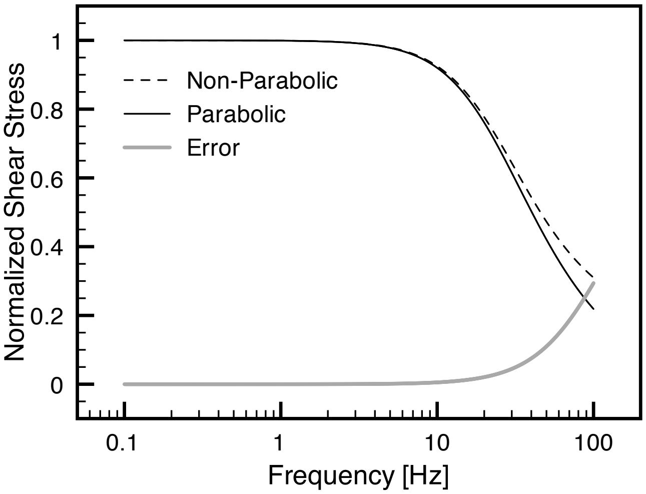

Figure S3 Calculations of shear stress for pulsatile flow at a constant pressure gradient amplitude. Shear stress is normalized to the highest value of the non-parabolic case. The results show that the amplitude of the fluid motion can be used to predict shear stress using an assumption of a parabolic flow profile with $<$ 5% difference below 32 Hz and $<$ 1% difference below 13.8 Hz.

$$\tau = \frac{6\mu Q}{bh^2} \tag{S5}$$

$$\tau = \frac{8\pi A f \mu}{h} \tag{S6}$$

Although Eq. S6 was used for all cell-based experiments where frequency was ≤ 2 Hz, the full pulsatile model was used during technical characterization. The equations used to the model the full pulsatile flow were previously presented in detail by Bacabac and co-workers.[7]

Shear Stress vs Voltage and Frequency

Characterization of shear stress as a function of frequency and voltage was carried out with a single microchannel that had exact dimensions of L × W × H = 7.5mm × 1.5 mm × 0.228 mm. Shear stress was estimated using particle motion. Particle motion was measured using 15 μm fluorescent beads (PN:F8843 - Invitrogen, Eugene, OR) with the same method outlined for shear stress calibration except with a 90-s wait time for bead settling as opposed to the 45-s wait time for cells. The microchannels were initially filled with PBS containing 0.5% BSA to prevent clumping of beads or adhesion of beads to channel walls. Exposure time was adjusted when necessary to capture a full period of particle motion for different frequencies. This method of shear stress determination becomes more challenging at high frequencies and amplitudes. At high amplitudes, the entire particle motion can extend beyond the viewfield of the microscope. At high enough frequencies ($>$ 20 Hz) acoustic streaming could be observed near edges or curved surfaces, and can disturb cell settling.[8] For significantly non-parabolic profiles, maximum fluid displacement does not occur at the center streamline. Although not quantified here, it is estimated that this effect could be noticed in the image sequences at frequencies above 20 Hz. Although challenges in shear stress determination can occur at high amplitudes and frequencies, overall, the method is repeatable (Fig S4b), fast, and appropriate for channel calibration in adhesion assays where physiological frequencies are $\sim$ 1 Hz and attachment occurs at shear stresses $<$ 1 Pa. In $\sim$ 2 min, shear stress in the channel can be determined and repeated to within a few pixels.

Experimental results illustrate the linear relationship between voltage and shear stress for three different frequencies while frequency is linearly related to shear stress below a frequency of 5 to 10 Hz at a voltage of 140 mV (Fig S4).

Excluding the frequency response of the actuator, there are two characteristic frequencies of the microchannel-diaphragm-actuator setup. The first dictates the transition from quasi-steady flow to pulsatile flow while the second marks a transition in the behavior of the pumping mechanism from behaving like a syringe pump to behaving like a regulated pressure source due to the compliance in the air space between the diaphragm and microchannel fluid. These transitions are discussed more fully in the next two subsections.

Flow Transition: Quasi-steady vs. Pulsatile. The Womersley number can be used to help characterize the pulsatile nature of the flow (Eq. S7) as it provides a measure of the balance between viscosity and momentum effects induced by oscillatory motion.

$$\Omega = a\sqrt{\frac{2\pi f \rho}{\mu}} \tag{S7}$$

In previous work by Bacabac and co-workers,[7] who compiled the information from Landau,[9] it is shown that the critical value for the Womersley number in PPFCs is 2.8, where the height of the PPFC is used as the representative length a. For our channel dimensions, Bacabac suggests shear stress will remain linear with pressure gradient below 4.8 Hz. This can be seen in Fig S5 where pulsatile flow shear stress is normalized by the quasi-steady flow result for the same pressure gradient. At low frequencies, the two models predict the same shear stress, whereas the pulsatile model attenuates above the transition frequency. Shear stress attenuates due to inertial effects induced by high frequency oscillations.

Pumping Transition. The ports and air chamber of the oscillatory flow setup act as capacitors with the microchannel acting as a resistance between them. At low frequencies, the capacitors are negligible and the volume displaced in the channel is

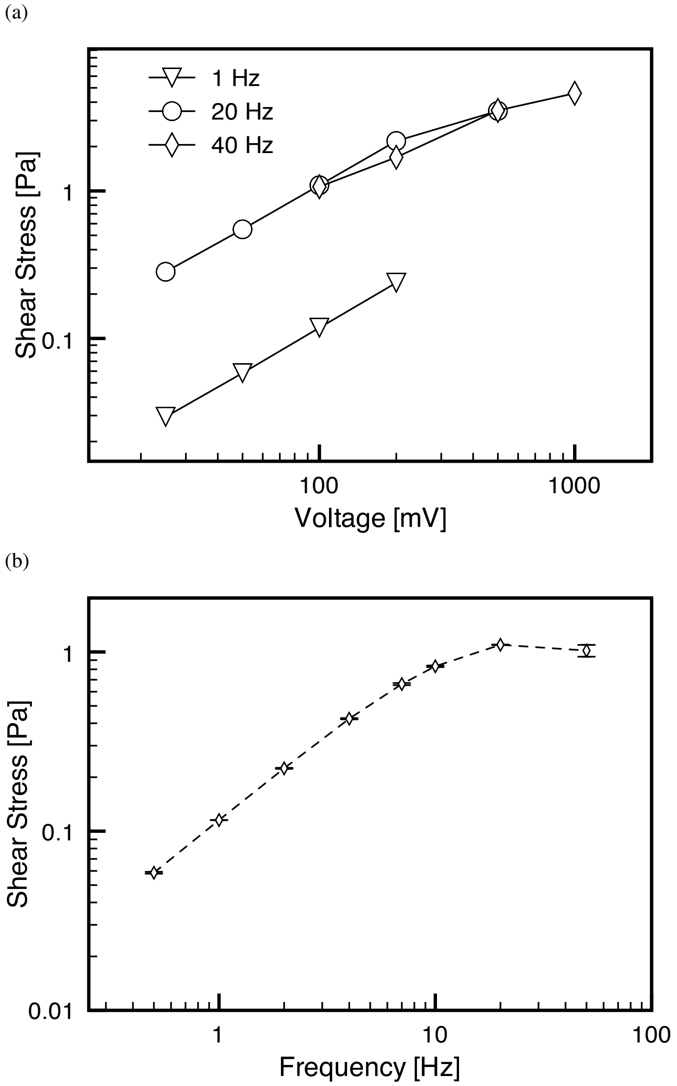

Figure S4 Shear stress in the device as measured by particle motion. (a) Shear stress was measured across a range of voltages for three different frequencies (Fig S4a). Each series of points indicates linear relationship between shear-stress and voltage, which is in agreement with simulation. Voltages refer to peak-to-peak signal levels that enters the piezo-amplifier. (b) Shear stress at a constant voltage of 140 mV. Actuator amplitude was constant below 16 to 32 Hz. The resonant frequency is > 80 Hz.

equal to the volume of air displaced in the sealed air chamber. At high frequencies, the resistance of the channel impedes charging and discharging of the capacitors, leading to a situation where fluid displacement is less than the air displaced in the air chamber. This can be seen in a plot of simulation results, where the ratio of the air displaced by the diaphragm is compared to the fluid displacement in the channel for a range of frequencies (Fig S5). At low frequencies, the pumping mechanism

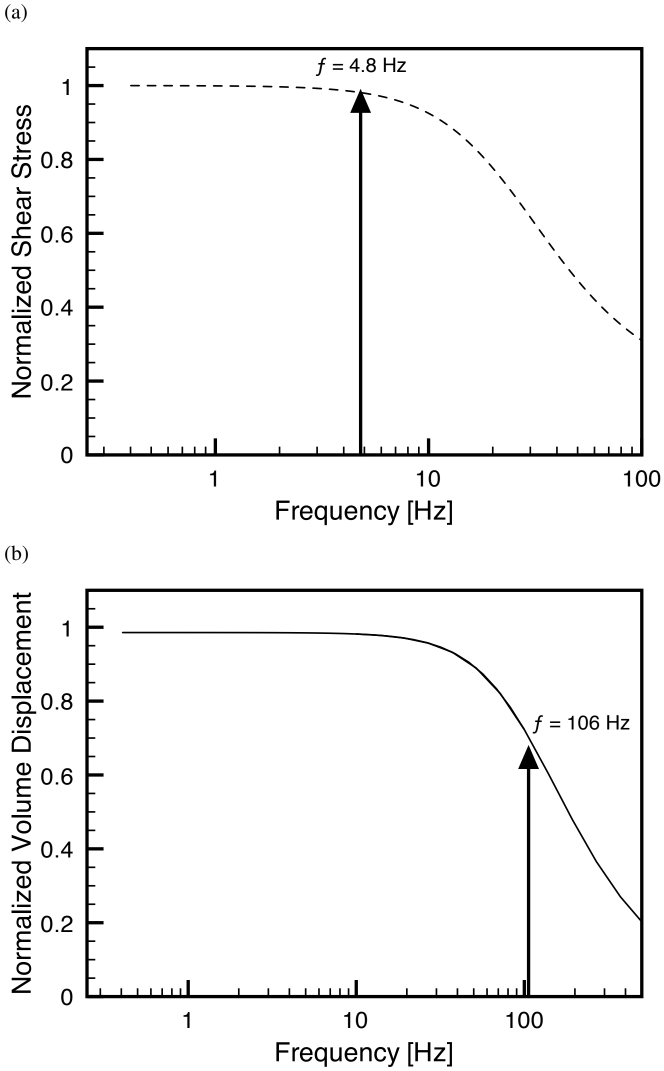

Figure S5 Simulations of transitions in device behavior. (a) Transition from steady to pulsatile flow. The influence of non-parabolic flow profiles can be seen on shear stress for frequencies above the transition frequency of 4.8 Hz. This simulation keeps pressure constant while varying frequency. The pulsatile flow shear stress calculation is normalized to the result found for the lowest frequency, which is nearly identical to the steady-flow solution for the same pressure gradient. (b) Transition from syringe-pump-like behavior to pressure-driven behavior. Normalized volume displacement represents the ratio of the air volume displaced by the actuator to the volume of fluid displaced in the channel. Simulation suggests that at low frequencies, the air and fluid displacement are tightly coupled with a ratio of almost 1. At higher frequencies, the capacitance of the air chamber coupled with the resistance of the microchannel result in a coupling that is less than 1.The capacitance of the air chamber and resistance of the channel suggest a pumping transition frequency of roughly 100 Hz which coincides with simulation results.

behaves much like a syringe pump and falls rapidly when above a certain cutoff frequency. This transition in the pumping behavior can be roughly estimated by calculating the capacitance of the air chamber ($C = 3.8 \times 10^{-13}$ [m^3/Pa]) and the resistance of the microchannel ($R = 3.95 \times 10^9$ [Pa-s/m^3]). The characteristic frequency of the transition can then be calculated using an RC-circuit analogy where $f = 1/(2RC) = 106$ Hz, which represents the frequency at which signal should be attenuated by roughly half. This calculation agrees well with results obtained from a numerical model of the actuator motion, pressurization of the air chamber and fluid flow. Although the transition is predicted to be near 106 Hz, the initial effects of the transition can be seen earlier, at $\sim$ 30 Hz. Still, the pumping transition frequency is well above the flow transition frequency; thus, the range where shear stress increases linearly with frequency is limited by the physics of pulsatile flow within the microchannel rather than the pumping mechanism. The pumping transition frequency can be increased if necessary by reducing the volume in the air chamber to create a stiffer capacitor (i.e., lower capacitance). At extremely high frequencies, the fluid displacement will be negligible compared to the air volume displaced by the diaphragm, resulting in what behaves like a pressure-based pump rather than a volume-based pump like a syringe pump where all lines are completely filled with fluid.

The simulation of Fig S5a agrees with the experimental data of Fig S4 that shear stress is linearly related to frequency below 5 Hz whereas above 5 Hz the influence of non-parabolic flow profiles and air chamber capacitance can be seen to influence the linear relationship.

Cell Culture

Human umbilical vein endothelial cells (HUVECs) were purchased from Lonza (Walkersville, MD), and regularly cultured on tissue culture-treated flasks precoated with 1.5 μg/cm^2 of bovine plasma fibronectin (FN) (Sigma-Aldrich, St. Louis, MO). HUVECs were maintained in EGM BulletKit media (CC-3124, Lonza) consisting of EBM-2 basal medium supplemented with 2% fetal bovine serum (FBS), bovine brain extract with heparin, hEGF, hydrocortisone, and gentamicin/Amphotericin B. HUVECs were fed every other day, passaged every 3-4 days at 90% confluence, and only passages 4-6 were used in microchannel experiments.

To prepare HUVEC monolayers for adhesion tests, microchannels were first primed with 30 μL PBS followed by 20 μL FN at 100 μg/mL concentration. Microchannels were incubated at 37°C for 1 h in humidified trays to allow FN adsorption to the microchannel walls. After incubation, FN was replaced twice with 40 μL HUVEC media further supplemented with 10 mM HEPES. HUVECs were seeded at 3000 cells/μL $\times$ 6 μL per microchannel, and allowed to adhere and culture overnight ($\sim$12 h). HUVEC microscale cultures were either used on the same day for adhesion tests if confluent, or maintained for an additional day to reach full confluence. Activated HUVEC monolayers in microchannels were induced with 10 μg/mL interleukin-1β (IL-1β; Cat. # 201-LB; R&D Systems Inc., Minneapolis, MN) for 4 h before adhesion tests.

Three different human cancer cell lines were used in adhesion tests to compare adhesion strengths on activated versus non-activated endothelium. MDA-MB231 cells (mammary gland epithelial) were maintained in DMEM with 4.5 g/L glucose supplemented with 10% FBS and 1% penicillin/streptomycin (P/S). PC-3 MM2 cells (metastatic prostate) were maintained in RPMI1640 with L-glutamine, 10% FBS, 1% P/S, and 10 mM HEPES. RPMI8226 cells (multiple myeloma in bone marrow) were maintained in DMEM with 4.5 g/L glucose supplemented with 10% FBS, 1% P/S, and 10 mM HEPES. MDA-MB231 and PC3-MM2 cells were fed every other day and passaged every 3-4 days depending on confluence. RPMI8226 cells were passaged every 3 days. All cell lines were resuspended at 500 cells/μL, and 5 μL of cell suspension was dispensed into each microchannel. Thus, each microchannel was delivered approximately 2,500 cells.

HUVEC Immunostaining

Immunostaining was performed to verify upregulation of E-selectin upon activation using IL-1β. After 4 h of 10 ng/mL IL-1β treatment, HUVECs were fixed with 4% paraformaldehyde, permeabilized with 0.1% Triton X-100, and immunostained with monoclonal anti-human E-selectin antibody (Clone 13D5, R&D Systems) and Hoechst 33342 nuclear dye (H1399, Invitrogen, Carlsbad, CA). Images of the stain were acquired on a Nikon Eclipse Ti inverted fluorescence microscope (Nikon Instruments, Melville, NY) with a Nikon DS-Qi1Mc CCD camera (Nikon Instruments).

Animals

Animals were purchased through Harlan Laboratories. All procedures were carried out in accordance with protocols approved by the University of Wisconsin School of Medicine and Public Health Animal Care and Use Committees.

Isolation of Cardiac Fibroblasts

The technique for isolating cardiac fibroblasts is adapted from previously published reports[10,11]. Briefly, male Lewis rats (260 to 400 *g*) were sacrificed by CO_2 asphyxiation, hearts rapidly excised, atria removed and ventricles placed into ice cold PBS with 1% P/S. Hearts were finely minced, and then placed into 10 mL digestion media (DMEM, 73 U/mL collagenase 2, 2 μg/mL pancreatin (4x)) and incubated at 37°C with agitation for 35 min. The digest mixture was centrifuged at 1000$\times g$ for

20 min at 4°C. The resulting cell pellet was suspended in 10 mL of fresh digestion media and incubated at 37°C with agitation for 30 min. The resulting digest was sieved through a 70 μm cell strainer and digest solution diluted with 10 mL of culture media (DMEM, 10% FBS, 1% P/S). The cell suspension was then centrifuged at $1000\times g$ for 20 min at 4°C. The cell pellet was suspended in 16 mL culture media and plated into two T75 culture flasks (8 mL per flask). The cells were allowed to attach under standard culture conditions (37°C, 5% CO_2, 100% humidity) for 2 h, then non-adherent cells removed by washing with PBS and culture media replaced. Primary cardiac fibroblast cultures were typically confluent in 4-7 days.

Generation of Cardiac Fibroblast 3D-ECM

Cardiac fibroblasts were seeded at a confluent density into the microfluidic devices and cultured in DMEM + 10% FBS and 1% P/S under standard culture conditions (37°C, 5% CO_2 and 100% humidity) for 2 h, then the open ports were scrapped free of cells to isolate the 3D-ECM to the device channel. Cardiac fibroblasts were cultured for 10 ± 3 days before decellularization using one of the following 3 methods abbreviated as CF, AH, and PAA. All adhesion experiments were carried out in serum-free DMEM.

Mock (CF) The cardiac fibroblasts were given a mock decellularization protocol of three washes with serum-free DMEM.

Ammonium Hydroxide/Triton X-100 (AH) Cardiac fibroblasts were removed from the secreted ECM by incubation with 20 mM ammonium hydroxide + 0.1% Triton X-100 (AH buffer) for 24-48 h at 4°C with constant agitation. The resulting matrix was then rinsed repeatedly with sterile water, then PBS, and finally washed 3 times with serum-free DMEM. For this method, the cardiac fibroblasts were plated onto Type I collagen-coated microchannels, which anchors the ECM to the channel, eliminating ECM liftoff during decellularization.

Peracetic Acid (PAA) Cardiac fibroblasts were removed from the secreted ECM by incubation with 0.15% peracetic acid (PAA buffer) for 24-48 hours at 4°C with constant agitation. The resulting matrix was then rinsed repeatedly with sterile water, then PBS, and finally washed 3 times with serum-free DMEM. PAA does not remove the matrix from the surface of the plate. Thus, Type I collagen was not required to anchor the matrix to the dish.

Isolation of Bone Marrow Stromal Cells

The technique for isolating bone marrow stromal cells (BMSCs) was adapted from previously published reports[11],[12]. Briefly, male Lewis rats (260-400 *g*) were sacrificed by CO_2 asphyxiation. Femurs and tibias were bilaterally excised and soft tissue removed. The bones were placed in ice-cold PBS with 1% P/S. In a sterile culture hood, the ends of the bones were removed, and an 18-gauge needle and syringe were used to flush the shafts of the bones with culture media (DMEM, 10% FBS, 1% P/S). The resulting bone marrow was further dispersed by passage through a 21-gauge needle. Cell suspension was then centrifuged at 1000 rcf for 10 min at 4°C and plated into a 100-mm culture dish. The cells were allowed to attach under standard culture conditions (37°C, 5% CO_2, 100% humidity) for 24 h. Non-adherent cells were removed by washing with PBS and replacing the culture media.

Although there are no established markers for the adult stem cells in the bone marrow stromal population, CD29, CD44, and c-Kit have been used by others. Immunostaining images of cells obtained using the above enrichment procedure are shown in Fig S6.

Image Capture

Phase contrast images were acquired at 2X with 2 × 2 binning and 15-ms exposure. The Ph1/PhC phase rings were used to provide maximal contrast (i.e., dark background and bright cells).

Prior to data acquisition, the calibration procedure (described above) was performed to measure the initial shear stress of the system at 140 mV piezo voltage and 2 Hz sinusoidal oscillation frequency. After calibration, 5 μL were removed from the input port followed by addition of 5 μL of cell suspension ($\sim$2500 cells) to the input port. The actuator was gently tapped to redistribute cells into the microscope field of view. After waiting 45 s for cells to settle, the acquisition protocol was started.

MetaMorph was used to acquire 46 image streams at specified intervals of time using the journaling capability of the software. The first 5 streams were acquired at 2 Hz. At the start of the sixth stream (also at 2 Hz), a descending log frequency sweep was initiated, and lasted for 500 s, until the frequency had reached 0.1 Hz. The number of frames per stream was chosen to ensure capture of 1-2 cycles of fluid/cell motion, and ranged from 25 to 170 frames. Variable numbers of frames were used to limit the amount of data. The software also allows for the logging of times. The time at the beginning of each image stream was recorded to allow determination of the exact frequency at a given time during acquisition. This improved accuracy because MetaMorph was not able to perform each stream acquisition at precisely the same time for each channel due to variability in data read-write times.

(a) CD29

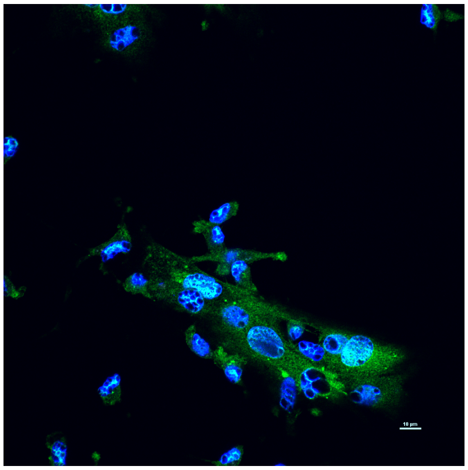

(b) CD44

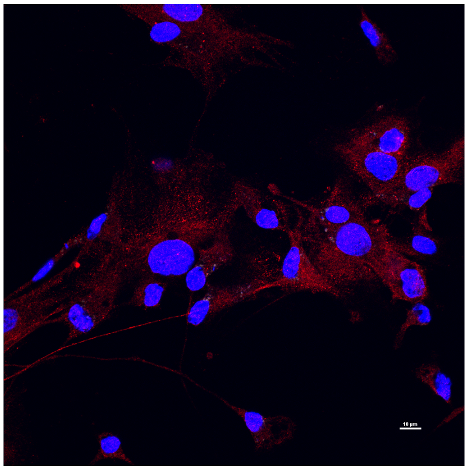

(c) c-Kit

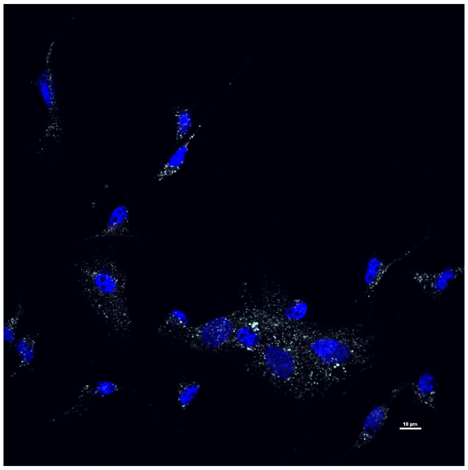

Figure S6 Immunostaining of bone marrow stromal cells from the same isolation procedure.

Descending Logarithmic Shear Stress Data Acquisition

The descending logarithmic sweep of frequency follows Eq. S8 where the frequency over time, $f(t)$, is defined in terms of the initial and final frequency, f_i and f_f, and the duration of the sweep, t_f.

$$f(t) = f_i \left(\frac{f_f}{f_i} \right)^{(t/t_f)} \tag{S8}$$

The logarithmic sweep was continuous rather than step-wise, which avoided any sudden pulses in shear stress. Shear stress was thus changing during each stream acquisition. However, the timescale for an adhesion event of a single cell was observed by us and others to be ~ 1 s (i.e., similar or less than the typical period of one oscillation).[13] Therefore, we assumed the number of adhered and non-adhered cells measured from an image stream was a valid representation of that time interval with a potential error similar to the difference between adjacent data points. This error is small compared to the changes in adhesion observed over the log sweep of shear stresses as demonstrated by the high R^2 values for each model fit (Table S1).

Image Analysis: Preprocessing

Background was subtracted from all images in the data set. The image used for background subtraction of each image stream was calculated from the first stream of images only. In phase contrast using low magnification (2X), cells appeared brighter than the background. The cells were introduced into oscillatory flow at the maximum shear stress of the assay so that they remained suspended. A stack projection is performed on the first stream to determine the minimum intensity for each pixel over time to ignore any bright moving objects (i.e., suspended cells) from the resulting background image. Thus, when the rest of the image streams were background subtracted using this image, the streams were greatly enhanced to show only cells that were initially added to the channel. Thus, any cells that were initially suspended at the beginning of the protocol can be seen throughout the image acquisition whether they are adhered or not. An Otsu automatic thresholding routine (available in Fiji) was used to threshold the enhanced images to produce binary images with cells appearing white over a black background. Background subtraction produced high contrast between cells and background to make the automatic thresholding routine robust. A single region of interest (ROI) is then chosen and applied to all images of the data set to restrict analysis to where shear stress is considered uniform. In this study, the center 80% of the channel width exhibited uniform shear stress and was chosen as the ROI. All subsequent analysis was limited to this ROI.

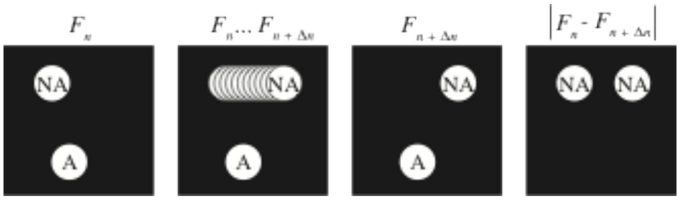

Figure S7 Image differencing algorithm. White circles represent cells in a binary image after image preprocessing. F_n refers to the n^{th} frame of an image stream. $F_{n+\Delta n}$ refers an image taken Δn frames after F_n. 'NA' refers to a cell that is not adhered, and 'A' refers to a cell that is adhered. $|F_n - F_{n+\Delta n}|$ represents the image that results from taking the absolute difference between F_n and $F_{n+\Delta n}$.

Image Analysis: Quantification of Percent Adhered Cells

Fig S7 shows a simple depiction of the black and white images that result from preprocessing. In any given frame of a stream, there can be adhered (A) and non-adhered (NA) cells. In a different frame of the same series, non-adhered cells appear at a different location, whereas adhered cells do not. If we take the absolute difference of these two frames, non-adhered cells would appear twice, whereas completely adhered cells would not appear at all. Thus, the integrated intensity of the difference image, Intensity($|F_n - F_n + \Delta n|$), is proportional to twice the number of non-adhered cells, whereas the integrated intensity of the reference frame, Intensity(F_n), is proportional to the number of total cells and we arrive at Eq. S9 for the percent of the population that is adhered where F_i represents the integrated intensity of the ith binary image..

$$\begin{matrix}\text{\% of Pop.}\\ \text{Adhered}\end{matrix} = 100\% \left(1 - \frac{\text{Intensity}(|F_n - F_{n+\Delta n}|)}{2 \times \text{Intensity}(F_n)}\right) \qquad \text{(S9)}$$

However, depending on how far apart in time these two frames are taken, a non-adhered cell in frame F_n may partially overlap with its new location in frame $F_{n+\Delta n}$. To address this, we first define a criteria for consistently choosing the reference frame, F_n. In this case, we chose the frame that has an integrated intensity that is closest to the average integrated intensity found for all the frames over the course of the image stream (Fig S7, left). The absolute difference between the reference frame and all other frames in the stream, $|F_n - F_{n+\Delta n}|$, are then calculated (Fig S7, right). The integrated intensity of the difference image plateaus to a maximum once the non-adhered cells in frame $F_{n+\Delta n}$ no longer overlap with there initial locations in frame F_n. During the sinusoidal motion of a non-adhered cell, overlap is expected to occur for less than than 30% of the cycle given the cell-size and minimum cell amplitudes. Therefore the top 5% of the difference values can be averaged to determine a final value for the numerator of Eq. S9. The single value obtained from the reference frame is used for the denominator. Some cells attached to the substrate exhibit a rocking motion as they are not completely adhered. The partial overlap produced by the rocking motion is accounted for in Eq. S9, providing a continuous measure of adhesion instead of a binary one that would indicated a cell as being either attached or not. This analysis is repeated for each of the 46 streams to produce 46 raw data points for each microchannel.

As mentioned previously, the first 5 image streams were acquired at 2 Hz. At the start of the sixth stream ($t = 0$ s, $f = 2$ Hz), a descending log frequency sweep was initiated. The average of adhesion data prior to 30 s was used to obtain an estimate of the maximum possible image-difference signal (i.e., when ~0% of cells are adhered). Note the minimum possible image-difference signal is zero and corresponds to 100% of the cells adhered. All difference signals were normalized to the maximum possible difference-signal estimate. Data points at times less than or equal to zero were averaged and plotted as a single point. This process was done for set of 46 raw data points to account for differences in the number of cells delivered to each channel.

Proper synchronization of the oscillation and image acquisition could be used to eliminate the need for image streams given that a proper choice for F_n and $F_{n+\Delta n}$ could be predicted based on the sinusoidal nature of the oscillation.

Data Fitting

The normalized data (percent of cells adhered vs. shear stress) was first fit using a least squares method with a single log-normal cumulative distribution function (F_{LN}, Eq. S10) to model the data as a single population. The fit determines an estimate for τ_{50} and σ that best represents the data, and an estimate of the goodness of fit of the single-population model, R^2_{single}. The quantity τ_{50} represents the shear stress at which half of the population is adhered (i.e., adhesion strength), whereas σ indicates the spread (i.e., heterogeneity), measured in orders of magnitude, of the data surrounding the median. The data is then fit with the weighted addition of two independent log-normal cumulative distribution functions (Eq. S11). α represents the percent of the population described by $F_{LN,a}$ whereas (1-α) represents the percent of the population described by $F_{LN,b}$. Thus, the resulting dual cumulative distribution still ranges between 0% and 100% as for the single-population model. Fitting with the dual-population model produces estimates for α, $\tau_{50,a}$, σ_a, $\tau_{50,b}$, and σ_b as well as an estimate of the goodness of fit for the dual-population model, R^2_{dual}. Single weighted values for τ_{50} and σ of the dual population model are calculated from $\tau_{50,a}$, σ_a, $\tau_{50,b}$, and σ_b according to the weighting distribution of Eq. S11. Thus, as α approaches 1 or 0, dual-population estimates of τ_{50} and σ converge to the same answer as the single-population model, while allowing one to account for the presence of two different populations for intermediate values of α. It should be noted that the least-squares fitting is dependent on a reasonable initial guess and all single- and dual-population model fits were verified visually in plots along with the fitted population parameters, τ_{50} and σ.

$$\begin{matrix}\text{\% of Pop.}\\ \text{Adhered}\end{matrix} = F_{LN}(\tau;\tau_{50},\sigma) = \frac{1}{2}\text{erfc}\left[\frac{\ln(\tau_{50}) - \ln(\tau)}{\sqrt{2}\sigma}\right] \quad \text{(S10)}$$

$$\begin{matrix}\text{\% of Pop.}\\ \text{Adhered}\end{matrix} = (\alpha)\, F_{LN,a} + (1-\alpha)\, F_{LN,b} \quad \text{(S11)}$$

The criterion for using the single- or dual-population model is based on R^2_{single} and R^2_{dual}. If the dual-population model demonstrates at least a 50% reduction in the remaining unexplained variability of the single-population model, then the dual-population model is used. Eq. S12 defines γ, the reduction in remaining unexplained variability. Thus, if $\gamma > 0.5$ then a dual-population model is used.

$$\gamma = \frac{\text{R}^2_{dual} - \text{R}^2_{single}}{100\% - \text{R}^2_{single}} \quad \text{(S12)}$$

One beneficial feature of using γ as a criterion is that it is sensitive to and limited by the ‘noise’ in the system. If intrinsic noise in the measurement limits the maximum possible R^2 of even the best model, it becomes harder to meet the criterion for adding a second population. This is in contrast to a ‘noiseless’ measurement method which would allow one to easily discern the parameters of even very small subpopulations.

However, the sampling rate of the data also affects the ability to observe subpopulations and should be taken into consideration when determining a realistic strategy for analysis. For example, a log-normal distribution is difficult to justify from three data points. Even if the sampling rate is sufficient for fitting of a log-normal distribution, extremely small values of σ can be a result of the fitting algorithm assigning a population to a step change observed between a few data points, and should be interpreted with caution. Thus, reasonable initial guesses for least-squares fitting are important.

Given the above cautions, this approach can be extended to more than 2 populations. Eq. S11 can be modified to include as many log-normal distributions as desired. However, the additional parameters added to the model will almost certainly reduce the error of the model fit. If too many populations are added to the model, over-fitting of the data can occur, leading to false identification of subpopulations. Additional populations will allow the model to better fit the noise in the data. Thus, one must still have a criterion for determining whether the additional population provides sufficient benefit to warrant inclusion. The criterion used here, γ, can be used to test the benefit of each additional population (i.e., 1 vs. 2 followed by 2 vs. 3, etc.). Further, manual verification of each model is always recommended, even in the case of very large data sets and automated analysis (e.g., plot comparison of the raw data and model fit as well as examination of population parameters, τ_{50} and σ).

Batch Processing

After the initial user input of ROIs to define the analysis region for each channel and the measurement of streakline lengths in each calibration image stream, the image filtering and analysis is completely automated using custom software called Je’Xperiment, developed by Warrick and Berthier at the University of Wisconsin Madison (http://sourceforge.net/projects/jextools). The software is used to database the images and perform batch processing of the custom algorithm. One array of 7 channels produces approximately 10-15 gigabytes of data. The primary time constraint of the analysis is thus the time it takes to read and write the images to a hard drive or server (∼5 hours total). However, Je’Xperiment allows one to obtain results for the array with only ∼20 min actually invested by the user at the computer workstation. Statistics are performed on these results using MStat (University of Wisconsin Madison, Department of Oncology).

Statistics - Differences in Measures vs. Substrate Condition per Cell Type

To determine significant differences in various measures (i.e., τ_{50}, σ, R^2_{dual} - R^2_{single}, or the number of populations needed to fit the data) between different adhesion substrates (i.e., HUVEC monolayers: activated and non-activated; Cardiac Fibroblast-derived ECM: AH, PA, CF), we used a combined Wilcoxon rank sum approach proposed by Lehmann[14]. The approach performs a rank test for each experiment per day, and assesses their combined significance. Data was considered statistically significant for $P < 0.05$.

Statistics - Differences in Measures vs. Tumor Cell Type per Substrate Condition

To determine significant differences in τ_{50} and σ between different tumor cell types on the same substrate, we performed independent Wilcoxon rank-sum tests on daily averages. This was done because not all comparisons had data that was gathered on the same day for the same experiment. This is in contrast to the comparisons made for different substrates, which made comparisons of the data collected in the same experiment and then combined the significance of the separate experiments. Data was considered statistically significant for $P < 0.05$.

2 Number of Cells Required for Population Characterization

As the proposed method is aimed at reducing the number of cells required to perform an adhesion assay, the following data illustrates how the signal changes as the number of cells analyzed changes. Three different channels were chosen that had significant adhesion by the end of the assay. The original ROI of height *h* [pixels] that was used to define the region of measurement for each channel was successively diminished in height (0.9*h*, 0.8*h*, 0.7*h*, 0.6*h*, 0.5*h*, 0.4*h*, 0.3*h*, 0.2*h*, and 0.1*h*) and reanalyzed to obtain new data curves. Fig S8 illustrates an example of the diminishing ROIs for one of the channels analyzed. It should be noted that this ROI affects the choice of the reference frame for quantification. Thus, this is a test of the overall algorithm and not just of the changes in raw signal from the ROI region.

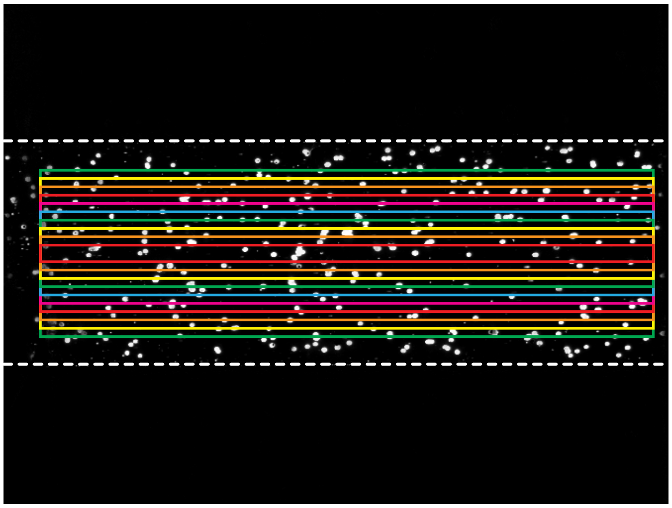

Figure S8 Different height ROIs are used to limit analysis to a smaller and smaller group of cells to observe how the signal from the assay changes as the number of cells diminishes.

The locations of the cells were manually selected in the image. The locations were then used to calculate the number of cells within the ROIs of different size. The 10 data curves obtained for each of the 3 channels analyzed are plotted in Fig S10. The legend indicates the number of cells that were analyzed to create each data curve.

Fig S10a, b, & c illustrate that the signal from the assay deviates most drastically from the rest of the data curves below 100 cells. Although the signal appears to deviate from the larger population at the lowest cell numbers, the overall strength of the signal does not attenuate appreciably as it is in terms of percent of the total observed population. As expected, when the height of the ROI is reduced, the analysis is no longer able

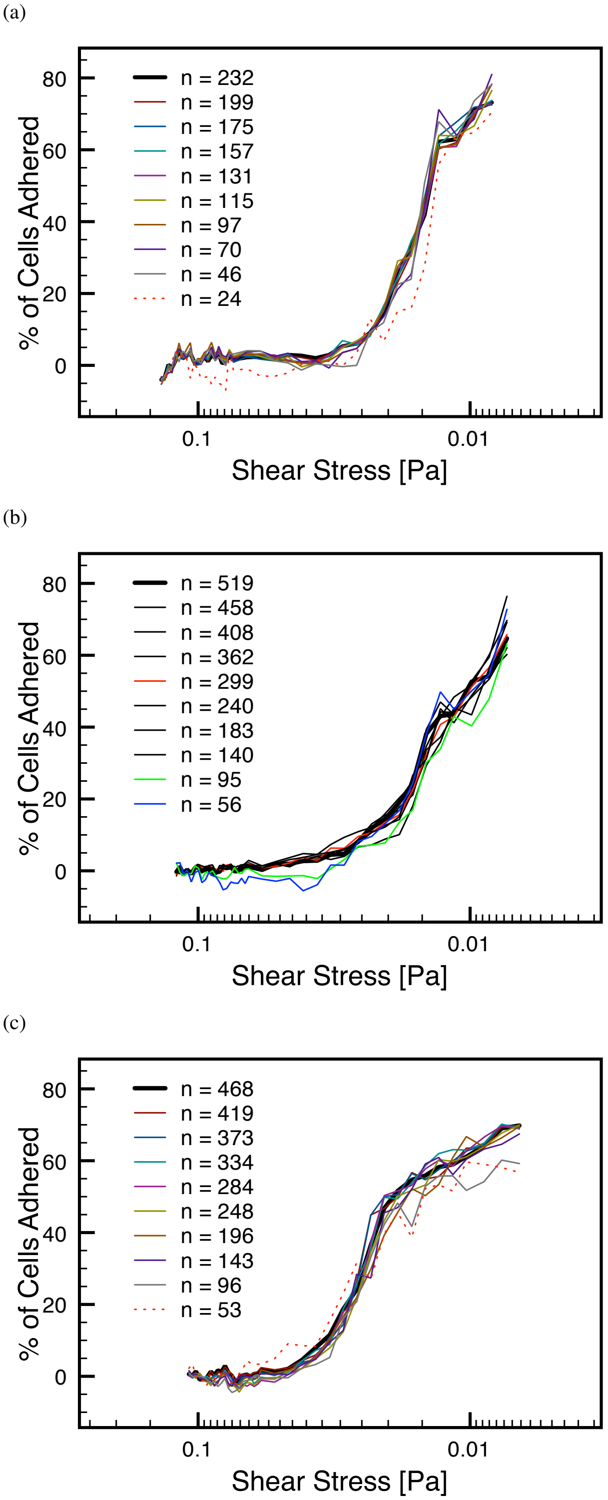

Figure S9 The signal from the adhesion assay is plotted for varying cell numbers for three different channels.

to ‘average out’ the heterogeneity. However, this does not mean that the signal is errant. In fact, a somewhat similar image differencing technique has been used to quantify the dynamics of single cell adhesion.[13] As the ROI shrinks our data becomes more and more like a single-cell measure. A larger ROI is chosen here to encompass many cells to simultaneously monitor many adhesion states at once to obtain population demographics with a single analysis region instead of one cell at a time. The number of cells needed to provide adequate coverage of the population is determined by statistical considerations and is necessarily on the order of $\sim$30-100 cells per population.

Taken together, Fig S10 supports our claim that we can analyze the population distribution of as few as 100 cells. The challenge is to load the cells as efficiently into the analysis region as possible. Currently about 20% of the cells that are loaded can be analyzed. However, this efficiency could become much closer to 100% through the use of a wider channel and alternate loading strategy such as a small diameter cell loading port nearer the analysis region to more directly deliver cells with minimal dead volume.

3 Data

See following pages.

(a) Top view

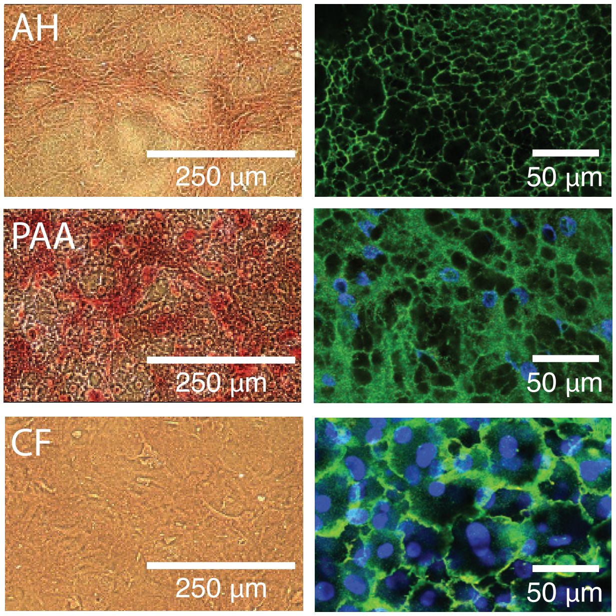

(b) Cross-section view

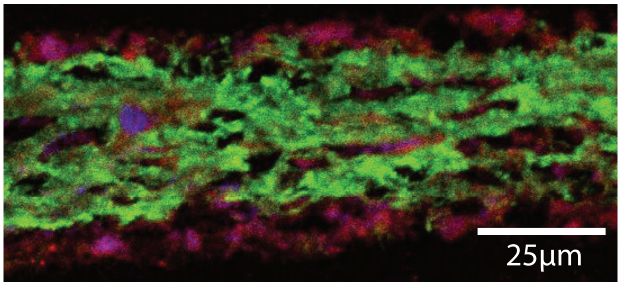

Figure S10 Enlarged color overlays of fluorescent immunostaining images contained Fig 3B of the main text.

Table S1 Summary of model fitting results for tumor cell adhesion experiments.

			Single Population Fit			***Dual Population Fit***								***Selection***		***Daily Averages***	
Expt. No.	*Cell Type*	*HUVEC Activation*	*Tau50*	*Sigma*	*R^2*	*Tau50_1*	*Tau50_2*	*Sigma_1*	*Sigma_2*	*Alpha*	*R^2*	*Tau50 Weighted*	*Sigma Weighted*	*Delta R^2*	*Single (1) or Dual (2)*	*Final Tau50*	*Final Sigma*
1	PC3	Y	0.01427	0.80573	0.97662	0.00388	0.02226	1.33710	0.40388	0.44421	0.99567	0.01410	0.81843	0.81481	2	0.01356	0.65748
1	PC3	Y	0.01229	0.72896	0.95698	0.00583	0.02240	0.68175	0.25536	0.56560	0.99000	0.01303	0.49653	0.76761	2		
1	PC3	N	0.00640	0.25375	0.84989	0.00640	-3.09E+04	0.25324	-9.80E+13	1.00935	0.84989	288.34952	9.16E+11	-0.00001	1	0.00640	0.25375
1	RPMI	Y	0.00276	2.21474	0.86991	0.00191	0.07853	1.63621	0.24622	0.87514	0.96357	0.01148	1.46266	0.71998	2	0.01236	1.47813
1	RPMI	Y	0.00267	2.37515	0.87256	0.00210	0.09622	1.66361	0.22661	0.88169	0.97067	0.01324	1.49360	0.76989	2		
1	RPMI	N	0.00170	1.84490	0.94001	0.00136	0.04135	1.49329	0.69869	0.92509	0.95469	0.00436	1.43376	0.24461	1	0.00106	2.23812
1	RPMI	N	0.00042	2.63135	0.82150	0.00310	0.06421	0.65266	0.39916	0.93233	0.89852	0.00724	0.63550	0.43152	1		
2	PC3	Y	0.01054	0.69696	0.91259	0.00648	0.02113	0.58278	0.27716	0.65924	0.93433	0.01147	0.47864	0.24876	1	0.01295	0.46119
2	PC3	Y	0.01139	0.91454	0.95522	0.00729	0.02284	0.01679	0.41876	0.48098	0.98922	0.01536	0.22542	0.75928	2		
2	PC3	N	0.00525	0.69592	0.95924	0.00533	0.03013	0.65201	0.00078	0.99071	0.96013	0.00556	0.64596	0.02183	1	0.00799	0.71423
2	PC3	N	0.00817	0.74980	0.98645	0.00677	0.01581	0.18022	0.42863	0.58352	0.99264	0.01054	0.28368	0.45674	1		
2	RPMI	Y	0.00178	2.18058	0.91150	0.00151	0.06052	1.40296	0.52277	0.88186	0.96719	0.00848	1.29897	0.62924	2	0.00924	1.42731
2	RPMI	Y	0.00221	2.20710	0.87709	0.00125	0.07561	1.71707	0.34700	0.88219	0.97634	0.01001	1.55565	0.80751	2		
2	RPMI	N	0.00098	1.87379	0.82062	0.00237	0.03337	0.69273	0.36544	0.91782	0.88361	0.00491	0.66584	0.35116	1	0.00098	1.87379
3	PC3	Y	0.01516	0.89251	0.97903	0.00217	0.02340	0.96745	0.57883	0.30013	0.99678	0.01703	0.69546	0.84638	2	0.01645	0.71446
3	PC3	Y	0.01555	0.81492	0.97484	0.00632	0.02598	1.08447	0.36173	0.51433	0.99603	0.01587	0.73345	0.84240	2		
3	PC3	N	0.00742	0.81886	0.98864	0.00601	0.01689	0.83160	0.29780	0.85559	0.99305	0.00758	0.75451	0.38801	1	0.00828	0.78842
3	PC3	N	0.00962	0.73252	0.98755	0.01520	0.00806	0.10655	0.87410	0.15128	0.99568	0.00914	0.75799	0.65307	2		
3	RPMI	Y	0.00288	2.06991	0.92185	0.00273	0.07673	1.53617	0.13817	0.91567	0.97493	0.00897	1.41828	0.67920	2	0.00871	1.41736
3	RPMI	Y	0.00305	1.92405	0.91783	0.00191	0.05199	1.57530	0.35938	0.86935	0.97189	0.00845	1.41645	0.65791	2		
3	RPMI	N	0.00150	1.72815	0.93095	0.00051	0.02363	1.88350	0.49440	0.90865	0.96135	0.00262	1.75660	0.44029	1	0.00186	1.92791
3	RPMI	N	0.00160	1.86947	0.94737	0.00059	0.02722	2.24903	0.25437	0.93916	0.97436	0.00221	2.12768	0.51279	2		
4	MDA	Y	0.01082	1.07123	0.96012	0.00366	0.02636	1.04412	0.47378	0.54821	0.99672	0.01391	0.78645	0.91785	2	0.01345	0.75432
4	MDA	Y	0.01010	1.03866	0.96912	0.00446	0.02500	0.88576	0.49180	0.58479	0.99175	0.01299	0.72219	0.73287	2		
4	MDA	N	0.00143	1.59105	0.86073	0.00332	0.05731	0.65948	0.20086	0.95748	0.93775	0.00562	0.63998	0.55307	2	0.00608	0.67067
4	MDA	N	0.00466	1.07192	0.96158	0.00521	0.00853	0.39470	1.15639	0.59740	0.98188	0.00655	0.70136	0.52830	2		
4	PC3	Y	0.00945	1.11381	0.97986	0.00234	0.02022	1.75741	0.60368	0.58705	0.98999	0.00972	1.28098	0.50288	2	0.01137	0.99422
4	PC3	Y	0.01121	0.94342	0.97613	0.00381	0.02243	0.92083	0.48959	0.50523	0.99541	0.01302	0.70746	0.80775	2		
4	PC3	N	0.00322	1.33588	0.95922	0.00326	3.65E+12	1.32498	-3.70E+13	1.00286	0.95917	-1.04E+10	1.06E+11	-0.00103	1	0.00650	0.89534
4	PC3	N	0.00717	0.69875	0.99005	0.00714	0.04753	0.67667	0.01011	0.99140	0.99017	0.00749	0.67094	0.01176	1		
4	PC3	N	0.00676	0.86523	0.98245	0.00676	0.05481	0.67517	0.18719	0.95124	0.99247	0.00910	0.65138	0.57117	2		
5	MDA	Y	0.00880	1.01076	0.97645	0.00070	0.01364	1.32387	0.75471	0.28422	0.98407	0.00996	0.91648	0.32361	1	0.00981	1.07743
5	MDA	Y	0.00970	1.04896	0.98322	0.00642	0.02007	1.34194	0.23582	0.81686	0.99351	0.00892	1.13937	0.61338	2		
5	MDA	Y	0.01129	1.02160	0.97546	0.00302	0.02446	1.49417	0.47863	0.59431	0.99363	0.01172	1.08217	0.74027	2		
5	MDA	N	0.00646	0.94434	0.98116	0.00645	0.05714	0.88931	0.00129	0.98602	0.98188	0.00716	0.87690	0.03822	1	0.00662	0.88404
5	MDA	N	0.00678	0.82374	0.98382	0.00693	0.07773	0.72142	0.08920	0.97939	0.99021	0.00839	0.70839	0.39510	1		
5	RPMI	Y	0.00210	1.91551	0.96124	0.00197	0.05990	1.59958	0.32934	0.94371	0.97852	0.00523	1.52809	0.44572	1	0.00893	1.28676
5	RPMI	Y	0.01145	1.09539	0.92898	0.00354	0.02754	1.04288	0.44657	0.50628	0.98007	0.01539	0.74847	0.71942	2		
5	RPMI	Y	0.00490	1.58103	0.97711	0.00373	0.05029	1.28098	0.57457	0.88016	0.98880	0.00931	1.19632	0.51060	2		
5	RPMI	N	0.00266	0.97481	0.97538	0.00281	0.03354	0.81725	0.15390	0.97689	0.98088	0.00352	0.80192	0.22339	1	0.00266	0.97481
6	MDA	Y	0.00722	1.17944	0.98399	0.00381	0.01725	1.62015	0.37378	0.80647	0.99025	0.00641	1.37894	0.39098	1	0.00766	1.14286
6	MDA	Y	0.00585	1.08602	0.97895	0.00355	0.01382	1.38426	0.45002	0.82340	0.98121	0.00536	1.21927	0.10704	1		
6	MDA	Y	0.01089	0.95346	0.97007	0.00326	0.02039	1.66616	0.36999	0.61190	0.98730	0.00991	1.16311	0.57565	2		
6	MDA	N	0.00445	1.31260	0.97922	0.00108	0.01571	1.32419	0.73352	0.65279	0.99215	0.00616	1.11910	0.62219	2	0.00605	1.14879
6	MDA	N	0.00594	1.17848	0.97872	0.00312	0.01473	1.61477	0.29936	0.81689	0.98878	0.00524	1.37390	0.47298	1		
6	PC3	Y	0.00916	1.21389	0.91662	0.00232	0.02927	1.68510	0.24562	0.68806	0.98938	0.01073	1.23607	0.87261	2	0.01248	0.98361
6	PC3	Y	0.01385	0.84754	0.95354	0.00533	0.02466	1.14769	0.24331	0.53942	0.99791	0.01424	0.73115	0.95508	2		
6	PC3	N	0.01253	0.50782	0.97758	0.01507	0.00227	0.25904	2.04480	0.63552	0.99179	0.01040	0.90992	0.63376	2	0.01225	0.75361
6	PC3	N	0.01428	0.69023	0.97318	0.00698	0.01934	1.24231	0.23867	0.50365	0.99629	0.01312	0.74415	0.86173	2		
6	PC3	N	0.01391	0.64381	0.97043	0.00834	0.02006	0.91609	0.17687	0.58156	0.99589	0.01325	0.60677	0.86113	2		

Table S2 Summary of model fitting results for cardiac adhesion experiments.

		Single Population Fit			***Dual Population Fit***								***Selection***		***Daily Averages***	
Expt. No.	*Substrate*	*Tau50*	*Sigma*	*R^2*	*Tau50_1*	*Tau50_2*	*Sigma_1*	*Sigma_2*	*Alpha*	*R^2*	*Tau50 Weighted*	*Sigma Weighted*	*Delta R^2*	*Single (1) or Dual (2)*	*Final Tau50*	*Final Sigma*
1	AH	0.02295	0.78630	0.97436	0.01145	0.02928	0.79495	0.37891	0.40034	0.99899	0.02215	0.54547	0.96069	2	0.02271	0.60607
1	AH	0.02143	0.62968	0.98747	0.00704	0.02869	0.91168	0.48054	0.37423	0.99448	0.02059	0.64188	0.55973	2		
1	AH	0.01855	0.79917	0.97611	0.00792	0.03540	0.92941	0.46046	0.36336	0.99654	0.02541	0.63086	0.85495	2		
1	PAA	0.00416	1.01790	0.98535	0.00427	0.04622	0.88804	0.34848	0.97713	0.98739	0.00523	0.87570	0.13913	1	0.00346	1.28731
1	PAA	0.00276	1.55672	0.96059	0.00276	-4.54E+14	1.55688	-7.92E+15	1.02149	0.96059	9.76E+12	1.70E+14	0.00000	1		
2	AH	0.00602	1.42270	0.96102	0.00452	0.02646	1.31058	0.99725	0.84604	0.96149	0.00790	1.26234	0.01196	1	0.00546	1.37659
2	AH	0.00602	1.34986	0.97410	0.00602	-4.29E+13	1.34979	4.06E+15	1.00745	0.97410	3.20E+11	-3.02E+13	0.00000	1		
2	AH	0.00434	1.35722	0.93784	0.00510	0.07245	0.90919	0.14711	0.94517	0.95451	0.00879	0.86740	0.26807	1		
2	PAA	0.00244	0.76285	0.30722	0.00248	4.64E+15	0.75565	5.69E+16	1.00782	0.30722	-3.63E+13	-4.45E+14	0.00001	1	0.00096	2.18476
2	PAA	0.00032	2.33468	0.89692	0.00032	2.99E+14	2.33451	4.01E+13	1.00168	0.89692	-5.03E+11	-6.75E+10	0.00000	1		
2	PAA	0.00012	3.45676	0.61986	0.00026	0.05786	1.89847	0.21197	0.92868	0.79960	0.00437	1.77819	0.47284	1		
3	AH	0.00317	1.61815	0.96031	0.00355	0.03120	0.66870	0.65083	0.81485	0.97360	0.00867	0.66539	0.33474	1	0.00365	1.56819
3	AH	0.00414	1.51823	0.96992	0.00279	0.03279	1.57359	0.37279	0.91833	0.98382	0.00524	1.47552	0.46214	1		
3	PAA	0.00059	2.44963	0.83685	0.00031	0.03824	1.49983	0.56083	0.88930	0.94086	0.00451	1.39588	0.63752	2	0.00182	1.96361
3	PAA	0.00055	2.05673	0.90907	0.00013	0.02335	2.45318	0.47401	0.95272	0.93748	0.00123	2.35960	0.31249	1		
3	PAA	0.00041	2.43824	0.86160	-0.00012	0.02802	4.94824	0.77846	0.89940	0.91295	0.00271	4.52877	0.37101	1		
4	AH	0.00572	1.15911	0.98354	0.00572	-1.45E+04	1.15912	-1.39E+15	1.00963	0.98354	1.39E+02	1.33E+13	0.00000	1	0.00629	1.10228
4	AH	0.00478	1.27091	0.97201	0.00548	0.08753	0.91451	0.18698	0.96188	0.98892	0.00861	0.88677	0.60394	2		
4	AH	0.00453	1.26095	0.97527	0.00439	0.03345	0.83209	0.51095	0.88420	0.97934	0.00776	0.79490	0.16452	1		
4	CF	0.00073	2.36763	0.88012	0.00073	9.80E+12	2.36774	5.74E+13	1.00862	0.88012	-8.45E+10	-4.95E+11	0.00000	1	0.00078	2.12570
4	CF	0.00109	1.68547	0.91545	0.00109	-1.03E+04	1.68540	-5.15E+14	1.00353	0.91545	3.64E+01	1.82E+12	0.00000	1		
4	CF	0.00052	2.32401	0.83375	0.00053	0.06494	2.01661	0.03472	0.97233	0.88540	0.00231	1.96176	0.31069	1		
5	AH	0.00399	1.46805	0.95863	0.00468	8.90E+02	1.19557	-9.79E+02	0.96559	0.96158	3.06E+01	-3.26E+01	0.07133	1	0.00274	1.80164
5	AH	0.00149	2.13522	0.93703	0.00230	0.10897	1.49145	0.15947	0.96429	0.96193	0.00610	1.44388	0.39541	1		
5	CF	0.00001	4.00251	0.45432	0.00000	0.04944	1.08946	0.59196	0.97192	0.58953	0.00139	1.07549	0.24778	1	0.00017	3.45800
5	CF	0.00044	2.56690	0.89103	0.00112	0.09764	1.59319	0.16979	0.96858	0.94024	0.00415	1.54847	0.45158	1		
5	CF	0.00006	3.80460	0.59384	0.00012	0.10441	2.40264	0.19189	0.95476	0.76114	0.00484	2.30263	0.41191	1		
6	AH	0.01480	0.96292	0.99099	0.00512	0.02380	0.35955	0.67405	0.32242	0.99872	0.01777	0.57265	0.85833	2	0.01621	0.71005
6	AH	0.01571	0.91359	0.98921	0.00023	1.94E-02	1.67200	7.83E-01	0.15131	0.99158	1.65E-02	9.17E-01	0.21904	1		
6	AH	0.01333	0.84192	0.97573	0.00489	0.02170	0.87146	0.49904	0.38905	0.99383	0.01516	0.64393	0.74577	2		
6	CF	0.00159	1.72327	0.95261	0.00037	0.01816	1.53481	0.76678	0.82645	0.97539	0.00346	1.40152	0.48062	1	0.00110	1.92903
6	CF	0.00082	2.04968	0.87697	0.00153	0.04660	1.17485	0.54253	0.94538	0.89632	0.00399	1.14031	0.15729	1		
6	CF	0.00088	2.01413	0.85196	0.00086	0.07474	1.87406	0.00033	0.98373	0.88018	0.00206	1.84358	0.19061	1		

References

[1] D. Duffy, J. McDonald, O. Schueller and G. Whitesides, *Analytical Chemistry*, 1998, **70**, 4974–4984.

[2] Y. Xia and G. Whitesides, *Angewandte Chemie-International Edition*, 1998, **37**, 551–575.

[3] K. Regehr, M. Domenech, J. Koepsel, K. Carver, S. Ellison-Zelski, W. Murphy, L. Schuler, E. Alarid and D. Beebe, *Lab on a Chip*, 2009, **9**, 2132–2139.

[4] S. Bhattacharyya and R. Pilipenko, *Characterization and Comparison of Control Units for Piezo Actuators to be used for Lorentz Force Compensation in the ILC*, Technical Report, http://lss.fnal.gov/archive/test-tm/2000/fermilab-tm-2454-td.pdf, 2010.

[5] C. Morris and F. Forster, *Experiments In Fluids*, 2004, **36**, 928–937.

[6] Y. Zeng, T. Lee, P. Yu, P. Roy and H. Low, *Journal of Biomechanical Engineering-Transactions of the Asme*, 2006, **128**, 185–193.

[7] R. Bacabac, T. Smit, S. Cowin, J. Van Loon, F. Nieuwstadt, R. Heethaar and J. Klein-Nulend, *Journal of Biomechanics*, 2005, **38**, 159–167.

[8] S. K. Chung and S. K. Cho, *Journal of Micromechanics and Microengineering*, 2008, **18**, 125024.

[9] L. D. Landau and E. M. Lifshitz, *Fluid Mechanics*, Permagon Press, Reading MA, 1959.

[10] R. K. Dubey, D. G. Gillespie, Z. Mi and E. K. Jackson, *Circulation*, 1997, **96**, 2656–66.

[11] H. Baharvand, M. Azarnia, K. Parivar and S. K. Ashtiani, *J Mol Cell Cardiol*, 2005, **38**, 495–503.

[12] P. Tropel, D. Noël, N. Platet, P. Legrand, A.-L. Benabid and F. Berger, *Exp Cell Res*, 2004, **295**, 395–406.

[13] K. Wang, X. Solis-Wever, C. Aguas, Y. Liu, P. Li and D. Pappas, *Analytical Chemistry*, 2009, **81**, 3334–3343.

[14] E. Lehmann, *Nonparametrics: Statistical Methods Based on Ranks*, Prentice Hall, Upper Saddle River, NJ, 1998.